

OPEN ACCESS

Ab Initio Insights to Metal Passivation: Diffusion and Defect Formation in Amorphous Zirconia and Alumina

To cite this article: Mackinzie S. Farnell et al 2025 J. Electrochem. Soc. 172 071502

View the article online for updates and enhancements.

You may also like

- Outstanding Platinum Recovery by Electrochemical Cathodic Leaching and Redeposition in One-Pot 2 M HCL Solution Mariappan Sakthivel, Reshma Gandharva, Christopher Schreiber et al.
- Conditional Wavelet Diffusion Models for High-resolution Solar Spectra Reconstruction of CHASE Data Cong Xiao, Jin Liu, Xin Ma et al.
- The Utility and Limitations of Distribution of Relaxation Times (DRT) Methods for Impedance Analysis Mark E. Orazem and Burak Ulgut

ECC-Opto-10 Optical Battery Test Cell: Visualize the Processes Inside Your Battery!



- Battery Test Cell for Optical Characterization Designed for light microscopy, Raman spectroscopy and XRD.
- Optimized, Low Profile Cell Design (Device Height 21.5 mm) Low cell height for high compatibility, fits on standard samples stages.
- High Cycling Stability and Easy Handling Dedicated sample holders for different electrode arrangements included!
- ✓ Cell Lids with Different Openings and Window Materials Available





Contact us:

+49 40 79012-734

■ sales@el-cell.com

www.el-cell.com









Ab Initio Insights to Metal Passivation: Diffusion and Defect Formation in Amorphous Zirconia and Alumina

Mackinzie S. Farnell, 1,2 Immy-Xuan Shen, 3 and Kristin A. Persson 1,2,2 Immy-Xuan Shen, 3 and Kristin A. Persson 1,2,2 Immy-Xuan Shen, 3 Immy-Xuan Shen, 3

Metal passivation refers to the formation of protective oxide films on metals, which shield them from further corrosion and oxidation, playing a crucial role in maintaining their stability. The mesoscopic Point Defect Model has successfully predicted passivity as a steady state process where oxide growth from oxygen vacancies at the metal/film interface competes with oxide dissolution at the film/environment interface. In this work, informed by the Point Defect Model parameters, we use first-principles calculations to calculate defect formation and atomic diffusion in amorphous materials and correlate these descriptors with the behavior and growth of the oxide film. Focusing on amorphous zirconia and alumina, we demonstrate that defect formation energies exhibit significant variability in amorphous systems. In alumina, vacancies dominate, with cation and anion vacancies occurring at comparable concentrations. Diffusion calculations for stoichiometric amorphous alumina and zirconia, as well as oxygen-deficient zirconia, reveal faster diffusion in the oxygen-deficient case, highlighting the impact of defects on transport. Comparison of calculated self-diffusion coefficients for the dominant defect species with experimentally measured oxide thicknesses shows a clear correlation, suggesting that first-principles-derived diffusivity information can serve as a key descriptor for surface passivation film growth.

© 2025 The Author(s). Published on behalf of The Electrochemical Society by IOP Publishing Limited. This is an open access article distributed under the terms of the Creative Commons Attribution 4.0 License (CC BY, https://creativecommons.org/licenses/by/4.0/), which permits unrestricted reuse of the work in any medium, provided the original work is properly cited. [DOI: 10.1149/1945-7111/adecc7]

Manuscript submitted April 22, 2025; revised manuscript received June 12, 2025. Published July 24, 2025.

Supplementary material for this article is available online

Metal passivation relies on the formation of a metal surface oxide film that protects the underlying metal from further degradation, effectively preventing harmful phenomena such as corrosion and oxidation. From a thermodynamic perspective, Pourbaix diagrams can be used to identify the specific potential-pH conditions that favor surface oxide formation. Importantly, using first-principles calculations to augment experimental data, Pourbaix diagrams have been shown to provide thermodynamic stability information about metastable and amorphous phases.^{2,3} When a surface oxide forms, the Pilling-Bedworth ratio predicts whether the oxide mechanically adheres to the metal without fracturing due to tensile or compressive stresses.⁴ Both Pourbaix diagrams and the Pilling-Bedworth ratio provide valuable information about a material's corrosion resistance and, importantly, can be calculated from first principles data which increases their applicability. ^{2,3,5-7} However, there are aspects of passivation that are inherently related to factors such as electric field, defect formation, and ionic diffusion, as discussed in recent perspectives, and shown in the Point Defect Model (PDM) that has been successfully applied to numerous systems.

The PDM theorizes passivation to be a kinetic phenomenon that depends on defect generation and annihilation reactions at the oxide/metal interface and oxide/environment interface and a dissolution reaction at the oxide/environment interface. P-11 Notably, the growth of the oxide film is driven by the oxygen vacancy generation reaction occurring at the oxide/metal interface. The passive film reaches a steady state thickness when the rate of film growth due to oxygen vacancies is equal to the rate of film destruction due to dissolution, thus the steady state thickness and current density can be determined from PDM parameters. Pully independent validation of the model is difficult because the model parameters are determined through fitting to experimental data, principally electrochemical impedance spectroscopy data. Recent work has also sought to use Mott-Schottky analysis and contact angle titration informed with first principles calculations to identify specific model parameters. Furthermore, the PDM has been used to calculate

the oxygen diffusivity, which can be compared to the diffusivity calculated from first principles. ¹³ Conversely, various authors have attempted to determine PDM parameters from first-principles calculations rather than fitting to experimental data. Hendy et al. studied cation transport through bulk crystalline iron oxide in the spinel phase. They compared their diffusion coefficients to an assumed diffusion coefficient used to fit Point Defect Model parameters and found the values agreed to within one order of magnitude. ¹⁴ Leung performed explicit interface calculations of crystalline phases of aluminum oxide on aluminum. These calculations provide new insights by accounting for interfacial effects and identifying the conditions that promote the formation of doubly charged oxygen vacancies, which are essential for oxide film growth according to the Point Defect Model. ^{15,16}

In this paper, we evaluate how first-principles defect formation energies and ionic diffusion coefficients for amorphous, stoichiometric and non-stoichiometric oxides relate to metal passivation within the context of the PDM. Defect formation energies are used to determine dominant point defects and their concentrations, and self-diffusion coefficients for dominant defect species are an essential descriptor of ionic transport. For our calculations, we focus primarily on amorphous oxides because several metals, such as aluminum and stainless steel are known to grow amorphous oxide films rather than crystalline films, ^{17–20} yet most prior first-principles studies focus on crystalline oxides.

Zirconia and alumina are studied as model systems because both metals form passivating surface oxide films that have been well characterized experimentally and computationally, which provides a good foundation on which to analyze our results. The zirconium surface films consist of a poly-crystalline inner layer of tetragonal zirconia and an outer layer of monoclinic zirconia. ^{21,22} Previous experimental studies indicate that amorphous grain boundaries several nanometers thick can form in zirconia films²³ and that diffusion rates are higher in zirconia grain boundaries compared to the grains themselves. ²⁴ Likewise, aluminum oxide films remain amorphous at low temperatures but crystallize as temperature rises. ^{17,18} Previous computational studies indicate that forming an amorphous aluminum oxide film is thermodynamically favorable. ²⁵

¹Department of Materials Science and Engineering, University of California, Berkeley, California 94720, United States of America

²Materials Science Division, Lawrence Berkeley National Laboratory, Berkeley, California 94720, United States of America ³Lawrence Livermore National Laboratory, Livermore, California 94550, United States of America

Here, we first present and discuss the details of the computational modeling, and compare to previous work. Specifically, given the variety of local environments in amorphous oxides, defect calculations are performed for several distinct sites to ensure good sampling of the possible configurations. Next, we present ionic diffusion coefficients from Ab Initio Molecular Dynamics (AIMD) for amorphous alumina and zirconia, including diffusion for an oxygen deficient, non-stoichiometric zirconia. The mechanism of diffusion is analyzed to determine how the local environment influences ionic mobility and lastly, the ionic diffusivity is compared to experimentally measured oxide thicknesses. ^{26–31}

Methods

Simulation details.—First-principles data was obtained using the Vienna Ab Initio Simulation Package (VASP)^{32,33} within the Perdew-Burke-Ernzerhoff generalized gradient approximation for solids (PBEsol)³⁵ implementations of density functional theory.³⁶ For AIMD, PBE was used with a plane-wave cutoff energy of 520 eV only sampled at the gamma point. PBEsol was used for structural relaxations prior to defect calculations and density of states calculations with a plane-wave cutoff energy of 680 eV and for defect calculations with a plane-wave cutoff energy of 500 eV. Systematic and robust calculations were facilitated using workflows based on Materials Project software infrastructure, including pymatgen³⁷, custodian³⁷, Fireworks³⁸, atomate³⁹, and atomate2⁴⁰.

Amorphous structure generation.—A simulated melt procedure using the mpmorph workflow in atomate was used to generate sample amorphous structures. ^{25,39,41} The AIMD calculations were run in an NVT ensemble using a 2 femtosecond timestep and the Nose Hoover thermostat. Initial configurations were created with Packmol to ensure a disordered, liquid-like starting state. 42 The structure's volume was equilibrated by performing AIMD simulations at varying volumes and fitting the results to an equation of state to estimate the ideal volume. This was followed by 2000-step AIMD simulations, with the volume adjusted between runs until the energy stabilized and the external pressure stabilized below 5 kilobar. After convergence, a 5000-step AIMD production run at 3000 K was conducted, and amorphous structures from this trajectory were sampled for diffusion and defect calculations. The AIMD parameters such as number of steps and criteria for energy and pressure stabilization were chosen based on Cheng et al. 43 Radial distribution functions of the structures are included in the Supplemental Information (SI) and indicate that our structures have similar bond lengths and coordination environments to prior work.²⁵,

Defect calculations.—To obtain low-temperature amorphous structures, two relaxations were performed prior to the defect calculations. ⁴⁰ Defect calculations were carried out using the defect workflow in atomate2, ^{40,47} with initialization and analysis facilitated by the pymatgen-analysis-defects package. ⁴⁸ Defect formation energies were determined from ⁴⁹:

$$E[\text{defect}] = E_{\text{tot}}[\text{defect}] - E_{\text{tot}}[\text{bulk}] - \sum_{i} n_i \mu_i + q E_{\text{F}} + E_{\text{corr}}$$

where E_{tot} [defect] represents the energy of the defective supercell, E_{tot} [bulk] is the energy of the bulk supercell, μ_i the chemical potential of adding or removing atoms, $E_{\rm F}$ the chemical potential of adding or removing electrons, and $E_{\rm corr}$ is a correction term to account for periodic boundary conditions. The Freysoldt correction is applied in this work⁵⁰ using dielectric constants for amorphous alumina and zirconia from Momida et al. and Zhao et al. ^{51,52} Bounds on the chemical potentials are set through the grand-canonical ensemble approach, as first defined by Zhang and Northrup, ⁵³ from zero-temperature energies of the bulk crystalline phases here referenced to elemental aluminum, zirconium, and oxygen. Within this framework, oxygen-rich chemical potential

conditions are represented by $\Delta\mu_O=0$ and metal-rich conditions by $\Delta\mu_M=0$. The Fermi energy was solved for using the py-sc-fermi package, ^{54,55} ensuring that the constraint for charge neutrality was satisfied. ⁵⁶ The density of states was calculated and used to self-consistently solve for the Fermi energy and is included in the SI.

Compared to crystalline structures, amorphous structures exhibit a wide range of atomic environments that have been observed to affect the defect formation energy. Therefore, several defect calculations are performed for different sites where sites were selected using different sample amorphous structure configurations (obtained at different times during the trajectory) as well as from varying local environments within the same sample structure. The interstitial positions were identified using an interstitial site finder, which locates the positions based on charge density analysis, benchmarked for crystalline systems. Reformed Prior computational studies indicate that point defect descriptions are valid for oxygen deficient amorphous alumina structures, showing that neutral oxygen vacancies exhibit defect states in the bandgap after AIMD and have associated structural configurations characterized by the formation of Al-Al bonds.

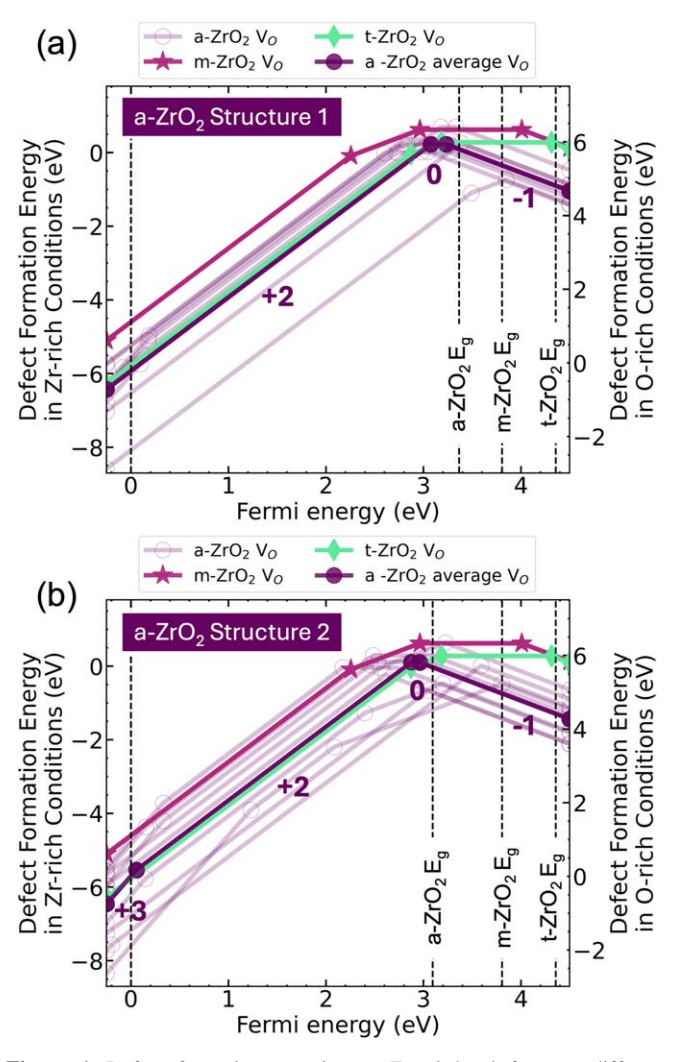


Figure 1. Defect formation energies vs Fermi level for two different amorphous zirconia structures referenced to oxygen rich and zirconium rich chemical potential reservoirs. Sites were randomly selected to ensure different sample coordination environments. The defect formation energies of various individual sites illustrate the distribution of formation energies and the variability in formation energy within the same amorphous structure. Formation energies for crystalline zirconia are the same across both plots.

Diffusion calculations.—To determine the diffusivity, AIMD calculations - using the same 2 fs timestep and thermostat - were performed for 30,000 time steps for alumina structures and 40,000 time steps for zirconia structures at temperatures ranging from 1900 K to 2800 K. The mean squared displacement (MSD) was calculated using the Einstein relation at each temperature for 3 different samples. To ensure that diffusivity was calculated correctly, the initial ballistic region of the MSD curve as well as the final poorly statistical sampled region of the MSD curve were excluded from fitting. An Arrhenius relation was used to extrapolate the diffusivity to lower temperatures. For non-stoichiometric, oxygen-deficient zirconium oxide, the electron count was adjusted. To investigate the diffusion mechanism in amorphous oxides, we employed the Density-Based Spatial Clustering of Applications with Noise (DBSCAN) algorithm^{62,63} which enabled us to identify atomic clusters at each step of the trajectory. ^{43,64–66} An atom was considered to vibrate, or stay immobile, when it remained in the same cluster, while an atom was considered to translate, or hop to a new location, if the atom moved to a different cluster between timesteps. The atom coordination numbers were used to approximate changes to the local environment and were calculated using the CrystalNN algorithm.⁶

Results and Discussion

In the following sections we report defect energies and associated diffusion constants for amorphous alumina and zirconia and discuss

how the results compare to prior available data on the stoichiometry and surface oxide growth, as relevant for metal passivation.

Defect formation in amorphous oxides.—For zirconium oxide, only oxygen vacancy formation energies were calculated, as surface zirconium oxide films are known to grow primarily through oxygen diffusion. ⁶⁸ Prior work suggests that zirconia films may feature an off-stoichiometric, oxygen-deficient inner layer, ^{29,69–71} with oxygen vacancies playing a crucial role in the growth of zirconium oxide layers, as proposed by the Point Defect Model. ⁷² Defect calculations were performed on amorphous as well as crystalline monoclinic and tetragonal zirconia, as these phases are known to feature in the passive layer on zirconium. ^{21,22}

Figure 1 shows the oxygen vacancy formation energies for two randomly selected amorphous zirconia structures with the crystalline defect formation energies included for comparison. The average defect formation energy of the amorphous structures is also included to illustrate the general trends. While the two amorphous structures exhibit similar ranges of defect formation energies, the primary difference is the narrow possibility of a +3 charge state in one structure under p-type conditions. Notably, we do not expect this extreme charge state to form because prior experimental work based on Mott-Schottky analysis found that the zirconium surface oxide layer typically exhibits n-type behavior.⁷³

Figure 1 shows that amorphous and crystalline zirconia exhibit similar trends, with oxygen vacancies favoring a +2 charge state at lower Fermi energies and transitioning to a 0 charge state at higher

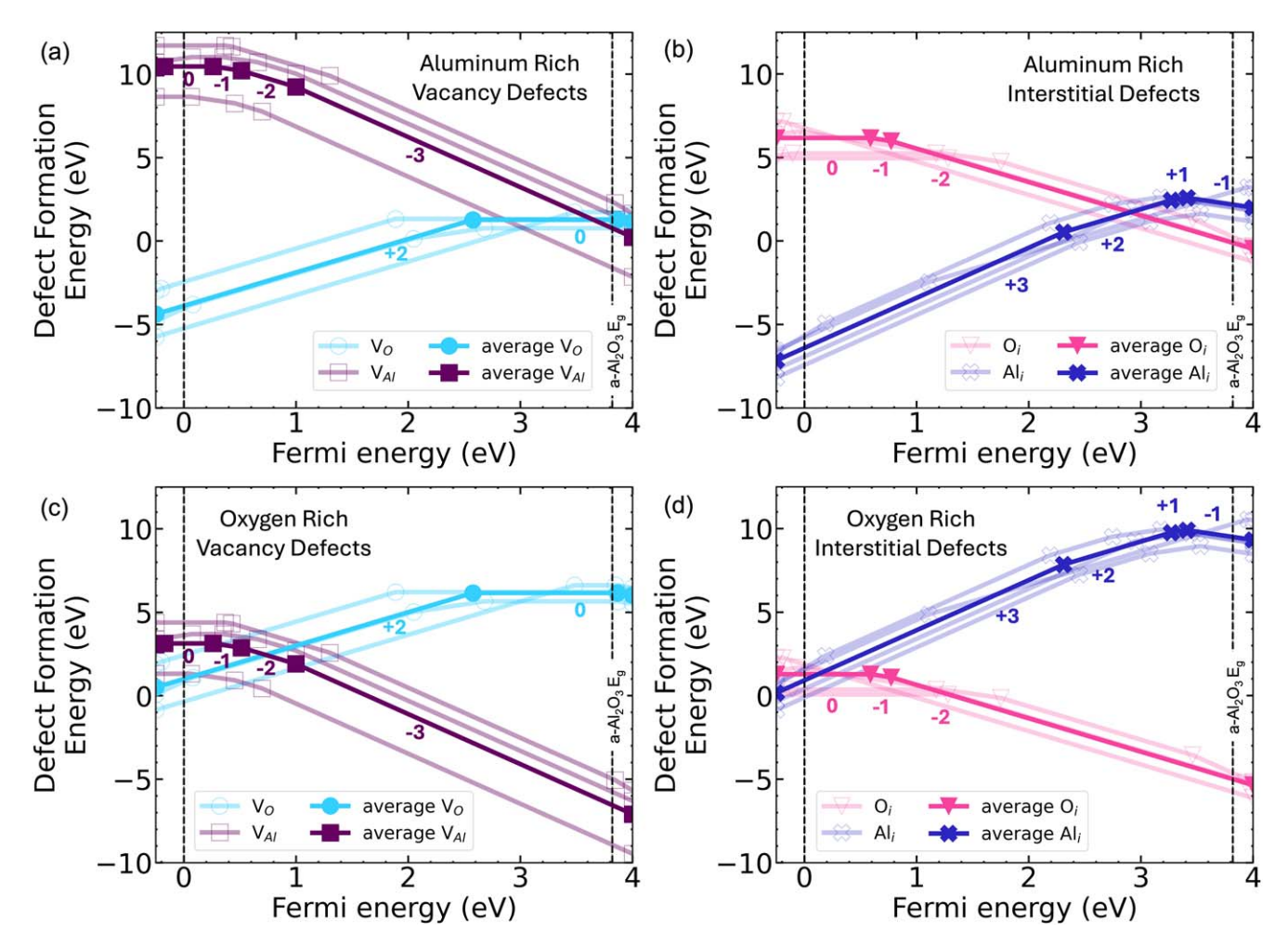


Figure 2. Defect formation energies vs Fermi level for vacancy (a) and (c) and interstitial (b) and (d) defects in one amorphous alumina structure referenced to aluminum rich chemical potential conditions (a) and (b) and oxygen rich chemical potential conditions (c) and (d). Sites were randomly selected to ensure different sample coordination environments. The defect formation energies of various individual sites illustrate the distribution of formation energies and the variability in formation energy within the same amorphous structure.

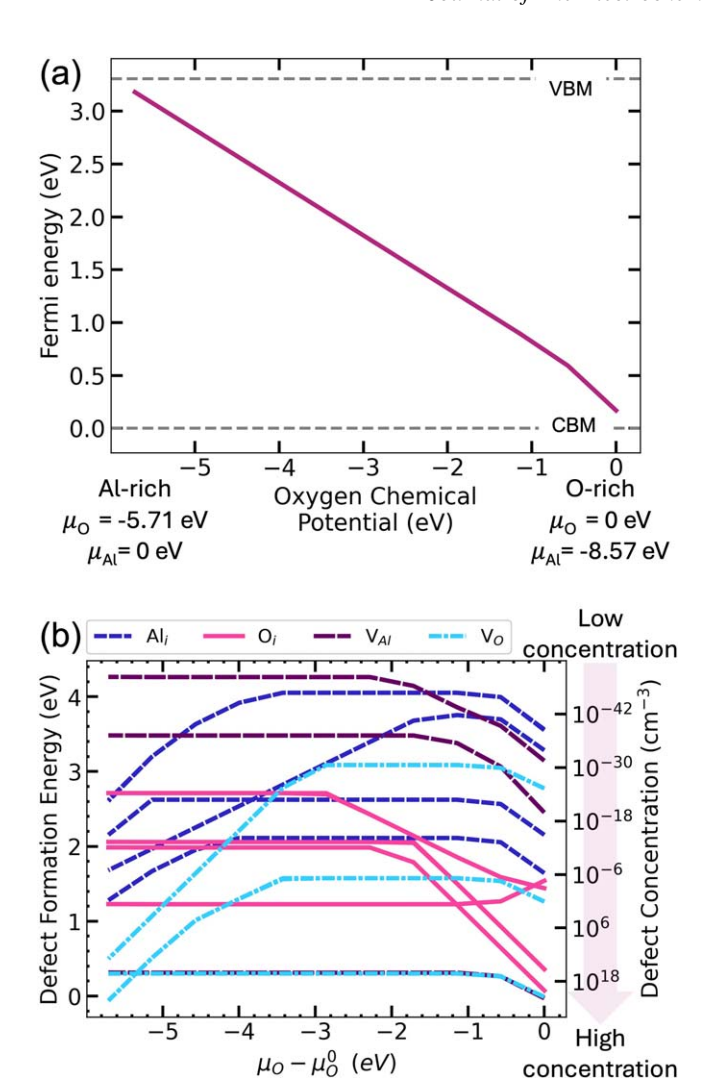


Figure 3. Fermi level vs oxygen chemical potential solved self-consistently at 300 K based on the constraint for charge neutrality (a), defect formation energy and concentration (b) vs oxygen chemical potential for all defects in amorphous alumina.

Fermi energies. On average, the defect formation energies in amorphous zirconia were comparable to those in tetragonal zirconia. However, amorphous zirconia included several sites with notably lower formation energies than those observed in either crystalline phase. These lower formation energies suggest that amorphous zirconia more readily accommodates oxygen vacancies, implying that amorphous regions in the passive layer are likely to be more oxygen-deficient than crystalline regions.

Several calculations of defect formation energies in crystalline zirconia have been performed previously for the tetragonal⁷⁴ and monoclinic^{75–77} polymorphs. Our results for tetragonal zirconia are in good agreement with the work of Youssef et al. although, we find a very narrow stability window (2.9 eV $< E_F < 3.1$ eV) for the +1 oxygen vacancy in disagreement with Youssef et al.⁷⁴ For monoclinic zirconia, our reported defect formation energies are comparable to previous authors, although different authors employ slightly different chemical potential conditions which leads to differences in the absolute energy values. 75-77 Zheng et al. and Shi et al. report negative-U behavior in monoclinic zirconia, where the +1 oxygen vacancy is never stable. 75,77 However, notably, the results of Van de Walle et al. align with our calculations, which show that the +1oxygen vacancy remains stable within a narrow range of Fermi levels. We suggest that these differences in the stability of the +1charge state result from the correction terms used to account for the

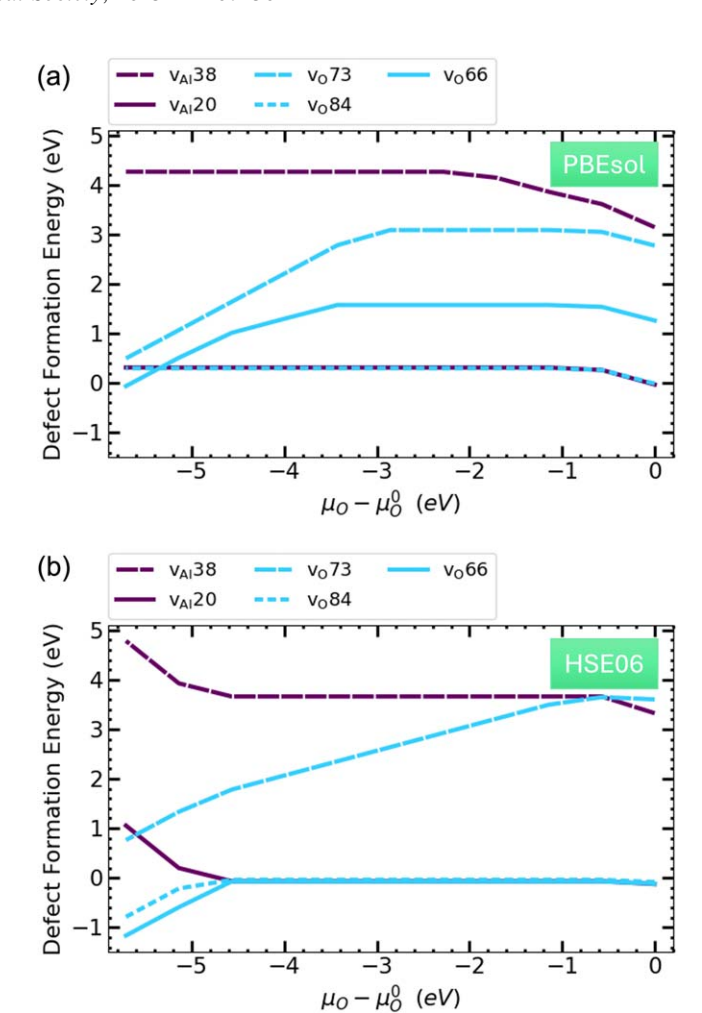


Figure 4. Defect formation energy vs chemical potential (300 K) for selected oxygen and aluminum vacancies in amorphous aluminum oxide calculated using two different functionals, PBEsol and HSE.

effects of periodic boundary conditions. This work and Van de Walle et al. use the Freysoldt correction in contrast to the other studies which use the Makov-Payne correction or no correction. ⁷⁶

As both aluminum and oxygen ions can contribute to the growth of the oxide layer, 68 the formation energies of the aluminum and oxygen vacancies, as well as aluminum and oxygen interstitials, were calculated in amorphous alumina. The defect formation energies for oxygen and metal rich chemical potentials are shown in Fig. 2, where we highlight the average defect formation energies in bold. The charge states for the oxygen vacancies are +2 or 0, with +2 being the most prevalent charge state, whereas the aluminum vacancies exhibit charge states from 0 to -3, with -3 being the most prevalent charge state. Both cation and anion vacancies generally exhibit lower formation energies than interstitials across most of the Fermi level range under both oxygen-rich and aluminum-rich conditions, indicating that vacancies are more likely to form in amorphous aluminum oxide. However, the interstitial formation energies are low enough to suggest that interstitials may also form.

We compare our results with the previously reported average defect formation energies in amorphous aluminum oxide by Dicks et al. ⁵⁷ The two studies differ insomuch that Dicks et al. employs the PBE0-TC-LRC functional and Lany and Zunger supercell correction, while the PBEsol functional and Freysoldt correction are employed in this work. While differences in electronic structure treatment and correction schemes lead to variations in absolute defect formation energies between our study and that of Dicks et al., key qualitative trends remain consistent. Both studies identify the

Table I. Ionic room temperature (293 K) self-diffusion constant in ZrO2, ZrO1,92 and Al2O3.

	ZrO_2	$ZrO_{1.92}$	Al_2O_3
Oxygen Ion Diffusion	$5.26 \times 10^{-19} \text{ cm}^{-2} \text{ s}^{-1}$	$1.67 \times 10^{-15} \text{ cm}^{-2} \text{ s}^{-1}$	$1.26 \times 10^{-27} \text{ cm}^{-2} \text{ s}^{-1}$
Metal Ion Diffusion	$1.34 \times 10^{-25} \text{ cm}^{-2} \text{ s}^{-1}$	$2.58 \times 10^{-16} \text{ cm}^{-2} \text{ s}^{-1}$	$2.98 \times 10^{-25} \text{ cm}^{-2} \text{ s}^{-1}$

oxygen vacancy in a +2 charge state that becomes neutral near midgap, and the aluminum vacancy as predominantly -3, transitioning to -2, with a neutral state near the valence band for shallow defects. Our results also reveal a limited stability window for the -1 charge state of the aluminum vacancy, which was not reported by Dicks et al. For oxygen interstitials, both studies observe 0 and -2 charge states; however, we additionally find stability for the -1 state, whereas Dicks et al. report a +1 state. The aluminum interstitial exhibits +3, +2, and +1 charge states in both works, though we also observe a -1 state near the conduction band, while Dicks et al. report it as neutral. These minor discrepancies do not affect the overall qualitative conclusions regarding the most prevalent charge states and defects, while highlighting the variability of defect energetics in amorphous systems.

To determine the most prevalent defects in amorphous aluminum oxide, the Fermi level was solved for self-consistently over a range of chemical potential conditions at 300 K. Defect formation energies and defect concentrations vs chemical potential are shown in Fig. 3, which indicate that the lowest energy/highest concentration defects are aluminum and oxygen vacancies, and that oxygen interstitials may reach high concentrations only for very oxygen-rich conditions.

Given the known differences between GGA and hybrid functionals, we calculated a small set of oxygen and aluminum vacancies using the HSE06 functional to compare against the PBEsol results. The defect formation energies vs Fermi level are shown in the SI and defect formation energies vs chemical potential are shown in Fig. 4. Not surprisingly, the bandgap predicted by PBEsol is approximately 2 eV lower than that predicted by HSE06. The HSE06-calculated bandgap aligns more closely with the experimentally reported range of 5.6 to 6.8 eV. 78 Regarding defect formation energies, both HSE06 and PBEsol predict that the lowest-energy oxygen and aluminum vacancies exhibit nearly identical formation energies, suggesting that these vacancies will occur in comparable concentrations. Thus, qualitatively, the two functionals yield similar results. However, it should be mentioned that HSE06 predicts that the defect formation energies for the lowest-energy defects are approximately 0.5 eV lower than those obtained using PBEsol and that the lowest-energy HSE06 defects exhibit negative formation energies, which indicate spontaneous oxygen loss under these conditions. We attribute these anomalously low values to some of the intentionally sampled highly undercoordinated sites. For example, the oxygen vacancy at site 66 exhibits a coordination number of 2 whereas most oxygen atoms in the amorphous aluminum oxide exhibit coordination numbers of 3 or 4. For such undercoordinated sites, in general, we find that the HSE06 and PBEsol functionals predict significantly different formation energies e.g. >1 eV difference. This difference could be attributed to PBEsol's treatment of the gradient expansion for exchange energy, which was included in PBEsol's design to improve predictions of surface energy and other bulk properties in comparison to other GGA functionals. Given the design of PBEsol to predict more accurate energies for surfaces, which contain heavily undercoordinated atoms, PBEsol may be better designed to predict energies for heavily undercoordinated sites within the bulk structure as well.³⁵ Nevertheless, the average defect formation energies remain positive across most of the chemical potential range, consistent with physical expectations.

Ionic transport.—Diffusion calculations were performed only for the amorphous oxides. Many oxide passivation films form noncrystalline structures or exhibit highly disordered regions between the polycrystalline grains. ^{79,80} Tromans revealed through

thermodynamic analysis of estimated energy differences between crystalline and amorphous oxides that grain boundaries in oxides may be treated as amorphous.⁸¹ In the case of zirconia, specifically, prior computational work by Owens et al. has suggested modelling grain boundaries in zirconia surface oxides as amorphous zirconia.⁴⁵

Ionic diffusivity was calculated for stoichiometric compositions of alumina and zirconia as well as for a non-stoichiometric zirconia with a 1:1.92 ratio of zirconium to oxygen. An oxygen-deficient, non-stoichiometric zirconia was included to investigate how off-stoichiometry influences diffusion, motivated by prior studies that have reported non-stoichiometry in zirconium oxide layers.²⁹

The mean squared displacement vs time with the Arrhenius-fit for diffusion coefficients (see Table I) are shown in the SI and Fig. 5. The oxygen diffusion coefficient in stoichiometric zirconia is within 1 or 2 orders of magnitude of the diffusion coefficient reported for oxygen vacancy diffusivity in the passive layer on zirconium, as determined with Point Defect Model parameters. 72 Comparing stoichiometric alumina and zirconia, we find that alumina exhibits similar diffusion for the aluminum and oxygen ions, whereas the stoichiometric zirconia exhibits significantly faster diffusion of oxygen ions as compared to zirconium ions. Previous work has shown that ionic diffusion in amorphous oxides occurs via bondbreaking/bond-formation events. Hence, it is reasonable to correlate the coordination number of the ions to their mobility.⁴³ Indeed, zirconium ions exhibit a higher oxygen coordination number in comparison to aluminum ions, which rationalizes the lower mobility of zirconium ions in relation to oxygen ions.

The diffusion of both oxygen and zirconium ions is found to be faster in non-stoichiometric zirconium oxide. We hypothesize that non-stoichiometric zirconium oxide exhibits faster oxygen diffusion due to the introduction of additional under-coordinated sites that are available to traverse the structure. Furthermore, we observed faster zirconium diffusion in oxygen-deficient zirconia and suggest a cross-correlation between oxygen and zirconium atom dynamics. As oxygen ions diffuse, they leave zirconium atoms in undercoordinated environments, which will enhance zirconium mobility.

To better understand the mechanism of diffusion in these amorphous structures, we analyzed a random sample of five oxygen ions in stoichiometric zirconia trajectories run at temperatures ranging from 2000 to 2800 K. Neighboring analysis was performed using a DBSCAN clustering algorithm^{62,63} and CrystalNN.⁶⁷ The results are presented in Fig. 6, which includes an image illustrating the trajectory of a single oxygen atom and histograms depicting the distribution of nearest neighbors during atomic translations and

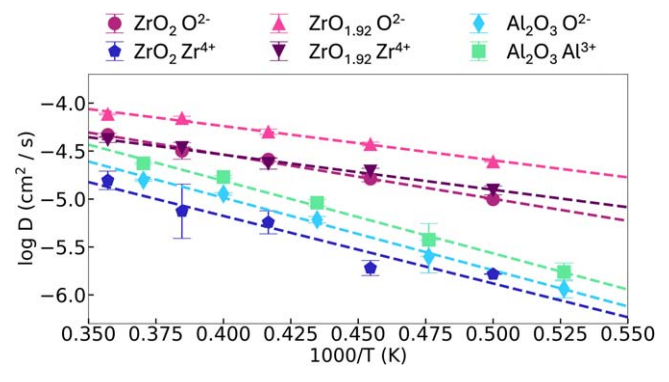
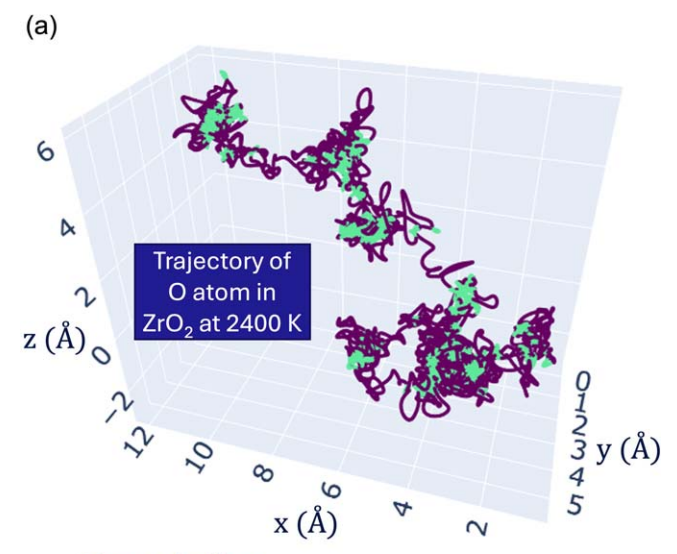
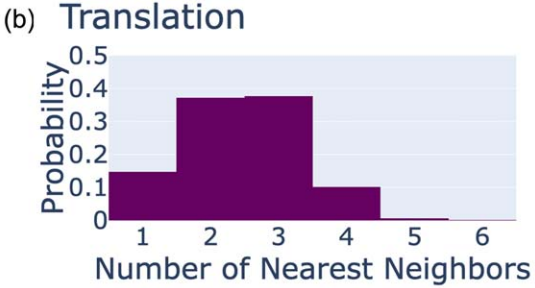


Figure 5. Arrhenius fit for diffusivity vs temperature for ZrO_2 , $ZrO_{1.92}$ and Al_2O_3 .





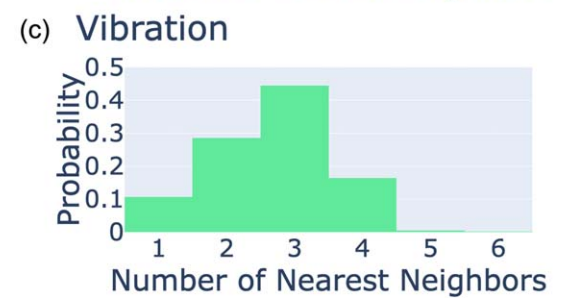


Figure 6. Schematic of trajectory for oxygen atom in ZrO_2 from a trajectory run at 2400 K (a), histogram showing probability for atom coordination number during translation (b), and histogram showing probability for atom coordination number during vibration (c).

vibrations. The histograms exhibit a slight skew, suggesting that atoms are more likely to adopt a lower coordination number when transitioning between local environments than when vibrating within the same environment.

To connect diffusion to the growth of the surface oxide, we surveyed existing literature for measurements of surface oxide thicknesses formed on aluminum and zirconium in oxygen environments. To allow comparability for thickness measured in different papers, we focused on measurements that were taken under low oxygen partial pressures in the initial stages of oxidation.^{26–30} The experimentally determined oxide thicknesses vs AIMD calculated diffusion values are presented in Fig. 7 and a table is included in the SI listing the references and oxygen partial pressures for each measured thickness. In some studies, a range of oxide thicknesses and/or temperatures is reported, and these ranges are included in the figure. In zirconia, oxygen vacancy defects and diffusion were identified as the dominant factors governing defect kinetics. Therefore, examining the correlation between the measured zirconia surface film thickness and the calculated oxygen diffusivity is most appropriate. Indeed, Davies et al. found that surface zirconium oxide growth is driven primarily by anion diffusion⁶⁸ using spectroscopy

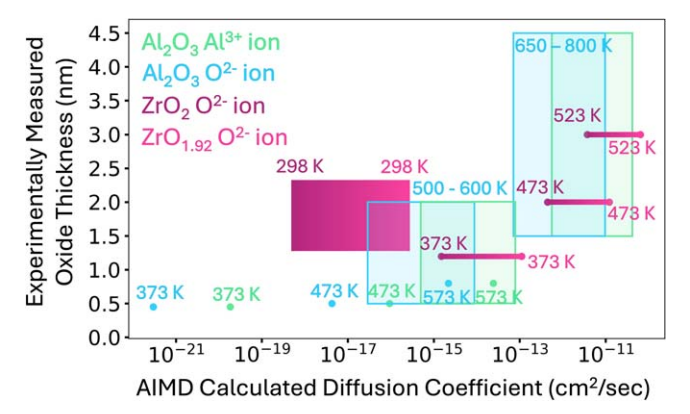


Figure 7. Plot of experimentally measured oxide thicknesses gathered from literature review vs oxygen diffusion coefficient calculated from ab initio molecular dynamics. Oxide thickness values were taken from References. ^{26–30}

and radiotracer techniques. While aluminum oxide may grow by either oxygen or aluminum ion diffusion, ⁶⁸ our calculations showed that oxygen and aluminum ions exhibit similar vacancy concentrations and diffusivity values. Thus, both oxygen and aluminum ion diffusion are included in Fig. 7.

The correlation between surface oxide thickness and the ionic diffusivity in the amorphous phase suggests that slower diffusion leads to thinner oxides while faster diffusion promotes thicker film growth. This aligns with the concept that diffusion is a key enabler for oxide film formation, such that a reduction in diffusion would naturally slow its growth rate. To fully capture growth dynamics of the film, it is recommended that future work investigate other factors such as ionic diffusion within crystalline grains of oxide, electric field effects, and defect concentrations at the interfaces. While this work focuses on diffusion in amorphous regions of the film, crystalline diffusion may become rate-limiting for thick oxide surface layers. For example, in the case of high temperature oxidation, considering the diffusion within crystalline grains may be relevant because films such as alumina are known to crystallize at higher temperatures. 17,18 Additionally, electric fields as a function of film thickness will affect the flux of charged species. Lastly, defect concentrations are likely to vary across the film and at interfaces, which are not considered here.

Conclusions

Defect formation energies and ionic diffusion coefficients for relevant defects have been calculated for amorphous zirconium and aluminum oxide to better understand how first-principles derived properties can inform growth of metal surface oxide films. Oxygen vacancy formation energies were calculated for both crystalline and amorphous zirconia and reveal that the amorphous zirconia has a wider range of defect formation energies and lower defect formation energies than crystalline zirconia. The results highlight the importance of studying multiple sites for defect calculations in amorphous phases and suggest that amorphous zirconia may more readily accommodate oxygen vacancies in comparison to crystalline zirconia. For amorphous aluminum oxide, defect formation energies were calculated for several possible defects, including oxygen vacancies, aluminum vacancies, oxygen interstitials, and aluminum interstitials. The calculations indicate that vacancies are often the lowest energy defects, and that oxygen and aluminum vacancies were similarly favorable.

Diffusion calculations were performed for stoichiometric amorphous alumina and zirconia and non-stoichiometric, oxygen deficient zirconia. Diffusion was found to be faster in the non-stoichiometric, oxygen deficient zirconia compared to the stoichiometric zirconia, which we hypothesize was due to the introduction of additional under-coordinated sites. The diffusion mechanism was analyzed to

assess the influence of the local environment on ion transport through the oxide and a correlation was observed between the local atomic environment and ion mobility. The self-diffusion coefficients for dominant defect species were compared to experimentally measured surface oxide thickness, revealing a positive correlation between diffusion and oxide thickness, with slower diffusion coefficients associated with the formation of thinner oxides. This result is intuitive, as diffusion influences the rate at which atoms reach the metal/film interface, facilitating the growth of the oxide film into the metal.

Acknowledgments

This work was enabled by the Berkeley Fellowship and Jane Lewis Fellowship from the University of California, Berkeley. This work was also supported with the Materials Project through the U.S. Department of Energy, Office of Science, United States, Office of Basic Energy Sciences, Materials Sciences and Engineering Division under Contract DE-AC02-05-CH11231: Materials Project Program KC23MP. Computational data was produced on the high performance computing systems Cori and Perlmutter at the National Energy Research Scientific Computing Center and Eagle and Swift at the National Renewable Energy Laboratory.

ORCID

Mackinzie S. Farnell https://orcid.org/0009-0002-8060-4762 Jianli Cheng https://orcid.org/0000-0002-0302-7861 Jimmy-Xuan Shen https://orcid.org/0000-0002-2743-7531 Kristin A. Persson https://orcid.org/0000-0003-2495-5509

References

- 1. M. Pourbaix, Corros. Sci., 14, 25 (1974).
- K. A. Persson, B. Waldwick, P. Lazic, and G. Ceder, *Phys. Rev. B*, 85, 235438 (2012)
- A. K. Singh, L. Zhou, A. Shinde, S. K. Suram, J. H. Montoya, D. Winston, J. M. Gregoire, and K. A. Persson, *Chemistry of Materials*, 29, 10159 (2017).
- N. B. Pilling and R. E. Bedworth, J. Inst. Met., 29, 529 (1923).
- A. M. Patel, J. K. Nørskov, K. A. Persson, and J. H. Montoya, *Phys. Chem. Chem. Phys.*, 21, 25323 (2019).
- 6. C. Zeng, A. Neils, J. Lesko, and N. Post, *Comput. Mater. Sci.*, 237, 112925 (2024).
- 7. C. Xu and W. Gao, *Mater. Res. Innov.*, **3**, 231 (2000).
- 8. A. Zagalskaya, P. Chaudhary, and V. Alexandrov, J. Phys. Chem. C, 127, 14587 (2023).
- 9. D. D. Macdonald, J. Electrochem. Soc., 139, 3434 (1992).
- 10. D. Digby, J. Electrochem. Soc., 153, B213 (2006).
- 11. D. Macdonald and G. Englehardt, ECS Trans., 28, 123 (2010).
- D. Chen, J. Pan, F. Mao, G. R. Engelhardt, C. Dong, and D. D. Macdonald, *Corros. Sci.*, 240, 112437 (2024).
- 13. E. Sikora, J. Sikora, and D. D. Macdonald, *Electrochimica Acta*, 41, 783 (1996).
- S. C. Hendy, N. J. Laycock, and M. P. Ryan, J. Electrochem. Soc., 152, B271 (2005).
- 15. K. Leung, J. Electrochem. Soc., 168, 031511 (2021).
- 16. K. Leung, J. Electrochem. Soc., 169, 081502 (2022).
- 17. J. Cui et al., Chemistry of Materials, 30, 7456 (2018).
- L. P. H. Jeurgens, W. G. Sloof, F. D. Tichelaar, and E. J. Mittemeijer, *Thin Solid Films*, 418, 89 (2002).
- 19. J. Kruger, Corros. Sci., 29, 149 (1989).
- M. P. Ryan, R. C. Newman, and G. E. Thompson, *J. Electrochem. Soc.*, **141**, L164 (1994)
- 21. Y. Ding and D. O. Northwood, Mater. Charact., 30, 13 (1993).
- C. M. Efaw, J. L. Vandegrift, M. Reynolds, B. J. Jaques, H. Hu, H. Xiong, and M. F. Hurley, *Corros. Sci.*, 167, 108491 (2020).
- 23. E. Rabkin, C. Y. Ma, and W. Gust, Mater. Sci. Monographs, 81, 353 (1995).
- 24. A. H. Chokshi, Scripta Mater, 48, 791 (2003).
- 25. M. Aykol and K. A. Persson, ACS Appl. Mater. Interfaces, 10, 3039 (2018).
- 26. C. O. De González and E. A. Garcia, Surf. Sci., 193, 305 (1988).
- B. E. Hayden, W. Wyrobisch, W. Oppermann, S. Hachicha, P. Hofmann, and A. M. Bradshaw, Surf. Sci., 109, 207 (1981).
- L. P. H. Jeurgens, W. G. Sloof, F. D. Tichelaar, and E. J. Mittemeijer, J. Appl. Phys., 92, 1649 (2002).

- 29. Y. Nishino, R. Alan, Y. Krauss, and D. M. Lin, J. Nucl. Mater., 228, 346 (1996).
- 30. L. P. H. Jeurgens, A. Lyapin, and E. J. Mittemeijer, Acta Mater, 53, 4871 (2005).
- A. Lyapin, L. P. H. Jeurgens, and E. J. Mittemeijer, "Effect of temperature on the initial, thermal oxidation of zirconium." *Acta Mater*, 53, 2925 (2005).
- 32. G. Kresse and J. Furthmüller, *Physical Review B*, **54**, 11169 (1996).
- 33. G. Kresse and J. Furthmüller, *Comput. Mater. Sci.*, **6**, 15 (1996).
- 34. J. P. Perdew, K. Burke, and M. Ernzerhof, Phys. Rev. Lett., 77, 3865 (1996).
- J. P. Perdew, A. Ruzsinszky, Gábor I Csonka, O. A. Vydrov, G. E. Scuseria, L. A. Constantin, X. Zhou, and K. Burke, *Phys. Rev. Lett.*, 100, 136406 (2008).
- 36. W. Kohn and L. J. Sham, Phys. Rev., 140, A1133 (1965).
- S. P. Ong, W. D. Richards, A. Jain, G. Hautier, M. Kocher, S. Cholia, D. Gunter, V. Chevrier, K. A. Persson, and G. Ceder, *Comput. Mater. Sci.*, 68, 314 (2013).
- 38. A. Jain et al., Concurr. Comput. Pract. Exp., 27, 5037 (2015).
- 39. K. Mathew et al., Comput. Mater. Sci., 139, 140 (2017).
- 40. A. M. Ganose et al., *Digital Discov.*, 4, 1944 (2025).
- M. Aykol, S. S. Dwaraknath, W. Sun, and K. A. Persson, Sci. Adv., 4, eaaq0148 (2018).
- L. Martinez, R. Andrade, E. G. Birgin, and J. M. Martinez, J. Comp. Chem., 30, 2157 (2009).
- J. Cheng, E. Sivonxay, and K. A. Persson, ACS Appl. Mater. Interfaces, 12, 35748 (2020)
- 44. P. Lamparter and R. Kniep, Phys. B: Condens. Matter, 234-236, 405 (1997).
- M. W. Owen, M. J. D. Rushton, L. J. Evitts, A. Claisse, M. Puide, W. E. Lee, and S. C. Middleburgh, J. Nucl. Mater., 555, 153108 (2021).
- 46. P. Li, I.-W. Chen, and J. E. Penner-Hahn, *Physical Review B*, 48, 10063 (1993).
- 47. J.-X. Shen, L. F. Voss, and J. B. Varley, J. Appl. Phys., 135, 145102 (2024).
- 48. J.-X. Shen and J. Varley, J. Open Source Softw., 9, 5941 (2024).
- C. Freysoldt, B. Grabowski, T. Hickel, Jörg Neugebaur, G. Kresse, A. Janotti, and C. G. Van de Walle, *Rev. Mod. Phys.*, 86, 253 (2014).
- C. Freysoldt, J. Neugebauer, and C. G. Van de Walle, *Phys. Rev. Lett.*, **102**, 016402 (2009).
- H. Momida, T. Hamada, Y. Takagi, T. Yamamoto, T. Uda, and T. Ohno, *Physical Review B*, 73, 054108 (2006).
- 52. X. Zhao, D. Ceresoli, and D. Vanderbilt, Physical Review B, 71, 085107 (2005).
- 53. S. B. Zhang and J. E. Northrup, *Phys. Rev. Lett.*, **67**, 2339 (1991).
- 54. A. G. Squires, D. O. Scanlon, and B. J. Morgan, J. Open Source Softw., 8, 4962 (2023)
- 55. J. Buckeridge, Comput. Phys. Commun., 244, 329 (2019).
- H. Yildirim, A. Kinaci, M. K. Y. Chan, and J. P. Greeley, ACS Appl. Mater. Interfaces, 7, 18985 (2015).
- O. A. Dicks, J. Cottom, A. L. Shluger, and V. Afanas'ev V, *Nanotechnology*, 30, 205201 (2019).
- 58. Y. Guo and J. Robertson, Microelec. Eng., 147, 254 (2015).
- 59. C. Tang and R. Ramprasad, *Physical Review B*, **81**, 161201 (2010).
- J.-X. Shen, M. Horton, and K. A. Persson, npj Computational Materials, 6, 1 (2020).
- 61. J. Strand and A. L. Shluger, Adv. Sci., 11, 2306243 (2023).
- M. Ester, H.-P. Kriegel, J. Sander, and X. Xu, KDD-96 Proc Second Int. Conf. Knowl. Discov. Data Mining, 96, 226 (1996).
- 63. F. Pedregosa et al., J. Mach. Learn. Res., 12, 2825 (2011).
- 64. W. Smith, G. N. Greaves, and M. J. Gillan, J. Chem. Phys., 103, 3091 (1995).
- 65. X. Lei, Y. Jee, and K. Huang, J. of Mater. Chem. A, 3, 19920 (2015).
- 66. S. C. Jung, H.-J. Kim, J. W. Choi, and Y.-K. Han, *Nano Lett.*, **14**, 6559 (2014).
- H. Pan, A. M. Ganose, M. Horton, M. Aykol, K. A. Persson, N. E. F. Zimmermann, and A. Jain, *Inorg. Chem.*, 60, 1590 (2021).
- J. A. Davies, B. Domeij, J. P. S. Pringle, and F. Brown, J. Electrochem. Soc., 112, 675 (1965).
- I. Bespalov, M. Datler, S. Buhr, W. Drachsel, G. Rupprechter, and Y. Suchorski, *Ultramicroscopy*, 159, 147 (2015).
- 70. D. Hudson, A. Cerezo, and G. D. W. Smith, *Ultramicroscopy*, **109**, 667 (2009).
- 71. Y. Dong, A. T. Motta, and E. A. Marquis, J. Nucl. Mater., 442, 270 (2013).
- J. Ai, Y. Chen, M. Urquidi-Macdonald, and D. D. Macdonald, J. Electrochem. Soc., 154, C43 (2007).
- Y. Chen, M. Urquidi-Macdonald, and D. D. Macdonald, *J. Nucl. Mater.*, 348, 133 (2006).
- 74. M. Youssef and B. Yildiz, *Physical Review B*, **86**, 144109 (2012).
- J. X. Zheng, G. Ceder, T. Maxisch, W. K. Chim, and W. K. Choi, *Physical Review B*, 75, 104112 (2007).
- C. G. Van de Walle, M. Choi, J. R. Weber, J. L. Lyons, and A. Janotti, *Microelec. Eng.*, 109, 211 (2013).
- L. B. Shi, Y. P. Wang, and M. B. Li, *Mater. Sci. in Semicond. Process.*, 27, 586 (2014).
- 78. S. Miyazaki, *J. Vac. Sci. Technol. B*, **19**, 2212 (2001).
- 79. J. W. Schultze and M. M. Lohrengel, *Electrochimica Acta*, 45, 2499 (2000).
- G. S. Frankel, J. D. Vienna, J. Lian, J. R. Scully, S. Gin, J. V. Ryan, J. Wang, S. H. Kim, W. Windl, and J. Du, npj Mater. Degrad., 2, 15 (2018).
- 81. D. Tromans, J. Electrochem. Soc., 152, B460 (2005).